

An elastic–plastic hybrid adhesion model for contacting rough surfaces in the presence of molecularly thin lubricant

Xi Shi, Andreas A. Polycarpou *

Department of Mechanical and Industrial Engineering, University of Illinois at Urbana–Champaign, Urbana, IL 61801, USA

Received 25 January 2005; accepted 20 April 2005

Available online 13 June 2005

Abstract

The study of adhesion has received considerable attention in recent years, partly due to advances in the design and fabrication of micro/nano devices. Many adhesion investigations are centered on single-spherical-contact models, which include the classic Johnson–Kendall–Roberts (JKR), improved Derjaguin–Muller–Toporov (IDMT), and Maugis–Dugdale (MD) models. Based on the IDMT single-asperity model, adhesive rough surface contact models have also been developed, which are valid for elastic and elastic–plastic contact conditions. A limitation of the IDMT-based models is that they are only valid for application cases with low adhesion parameter values. In this research, a contacting rough surface adhesion model was developed by combining an extended Maugis–Dugdale (EMD) model (which is only valid for elastic contacts) with an IDMT-based elastic–plastic adhesion model. The proposed model, termed the elastic–plastic hybrid adhesion model, is valid for the entire adhesion parameter range and also for elastic–plastic contacts. The proposed model gives results similar to the EMD rough surface model when the contact is primarily elastic. Moreover, the proposed model was compared to an IDMT-based model (ISBL model) and both gave similar results for contacts with low adhesion parameter values. With high adhesion parameter values, the ISBL model fails, whereas the proposed model correctly predicts higher adhesion. Last, based on the stiffness of the external force, the instability for adhesive rough surfaces in contact was also discussed, and it was postulated that a high peak value of the external force stiffness directly relates to the unstable contact process.

© 2005 Elsevier Inc. All rights reserved.

Keywords: Adhesive contact; Extended Maugis–Dugdale; Roughness; Elastic–plastic contact; Head/disk interface

1. Introduction

With rapid developments in micro/nano devices such as micro/nano electromechanical systems (MEMS/NEMS) and magnetic storage head–disk interfaces (HDIs), intermolecular adhesive interactions between two surfaces have become increasingly important and received considerable attention in the literature. These advances are coupled with the development of advanced instrumentation, such as the atomic force microscope (AFM), which enables detailed experimental investigations of adhesive problems down to molecular sizes. Concurrently, a physical understanding of interfacial adhesion directly influences the successful design and

implementation of microdevices such as the HDI interaction in magnetic storage hard-disk drives.

For single spherical elastic contacts, there are three major adhesion models. The first model, suggested by Johnson et al. [1], is known as the JKR model, and it assumes that the adhesive forces are confined only in the contact area and that these forces result in a larger contact area than that predicted by Hertz theory. The second model, due to Derjaguin et al. [2], is known as the DMT model, and it assumes that the adhesion forces act in a ring-shaped zone of the noncontact area; i.e., there is no adhesion from within the contact area, and the Hertz profile and thus the contact area does not change. Following a debate on which of the two models was correct, Tabor [3] pointed out that both models are correct and each model is valid under different conditions. Furthermore, the DMT model transitions to the JKR model

* Corresponding author. Fax: +1 (217) 244 6534.

E-mail address: polycarp@uiuc.edu (A.A. Polycarpou).

Table 1
Summary of single spherical adhesive contact models

Reference	Model acronym	Comments
[1]	JKR	<i>Johnson–Kendal–Roberts model:</i> <ul style="list-style-type: none"> • Adhesion is confined within the contact area • Adhesion results in a larger contact area than Hertzian contact • Valid for elastic contact only • Valid for high adhesion parameter only • Not considering noncontacting situations
[2]	DMT	<i>Derjaguin–Muller–Toporov model:</i> <ul style="list-style-type: none"> • Adhesion acts in a ring-shaped zone outside the contact area • Adhesion does not change the Hertzian profile • Valid for elastic contact only • Valid for low adhesion parameter only • Not considering noncontacting situations
[5]	IDMT	<i>Improved Derjaguin–Muller–Toporov model:</i> <ul style="list-style-type: none"> • Adhesion acts in a ring-shaped zone outside the contact area • Adhesion does not change the Hertzian profile • Valid for elastic contact only • Valid for low adhesion parameter only • Noncontacting situation was considered
[6]	KE	<i>Kogut–Etsion model:</i> <ul style="list-style-type: none"> • Adhesion acts in a ring-shaped zone outside the contact area • Surface profile was obtained by finite element analysis • Valid for elastic–plastic contact • Valid for low adhesion parameter only • Noncontacting situation was considered
[7]	MD	<i>Maugis–Dugdale model:</i> <ul style="list-style-type: none"> • Constant adhesive stress acts in a ring-shaped zone outside the contact area • Valid for wide adhesion parameter values • Valid for elastic contact only • Not considering noncontacting situations
[9]	EMD (SP)	<i>Extended Maugis–Dugdale model (Shi–Polycarpou):</i> <ul style="list-style-type: none"> • Constant adhesive stress acts in a ring-shaped zone outside the contact area • Valid for wide adhesion parameter values • Valid for elastic contact only • Noncontacting situation was considered

by adjusting the so-called “Tabor” adhesion parameter. Subsequent work by Muller et al. [4,5] numerically showed that indeed the JKR-to-DMT transition occurs through a dimensionless adhesion parameter, which is related to the Tabor adhesion parameter. In Ref. [5], they also extended their original work to the noncontacting situation, which is referred as the improved DMT (IDMT) model. Based on the IDMT model and using the finite element method, Kogut and Etsion [6] developed a single-asperity adhesion model, which is valid for elastic–plastic contact.

The third single-asperity adhesion model was developed by Maugis [7], where a continuous analytical transition between the JKR and IDMT models, using the Dugdale approximation, was developed. The Dugdale approximation assumes a state of constant adhesive stress over some length at the gap between a contacting sphere and a flat surface (i.e., modeled as a crack tip). Kim et al. [8] proposed an extension to the Maugis–Dugdale (MD) model for the case when the sphere is not in intimate contact with the flat surface but within the active adhesion range. In Ref. [8] they assumed a constant (theoretical) stress σ_0 for the noncontact condi-

tion, which overestimated adhesion and limited its effective range. Subsequently, Shi and Polycarpou [9] proposed another extension to the MD model for the noncontact situation based on the concept of adhesion work. This model, referred as the extended Maugis–Dugdale (EMD) model, overcomes the problems of [8]. Table 1 lists the single-spherical-adhesive-contact models discussed above, along with their acronyms, main features, and limitations.

As realistic interfaces possess roughness, one needs to extend the above single-asperity models to multiasperity models. For such cases, a widely used multiasperity contact model is the Greenwood and Williamson (GW) statistical contact model [10]. The GW statistical model has been widely accepted due to its clear physical interpretation and good agreement with experimental data (e.g., [11–13]), despite its shortcomings of scale dependency [14]. Chang et al. (CEB model) [15] developed an adhesion model for rough surfaces under dry contact conditions by combining the IDMT model with an extended GW model that included elastic–plastic contacts. Kogut and Etsion [16] developed a rough surface adhesion model (KE model) based on their

improved single-asperity model [6], in which case a more accurate (compared to Chang et al. [15]) deformed surface profile was obtained at different approach levels. An advantage of both CEB and KE models is that they are valid for elastic–plastic contact conditions. However, a major disadvantage of these models is that since they are based on the IDMT adhesion model, they are only valid for a limited range of low adhesion parameter values, which is unrealistic in many applications, such as MEMS and magnetic storage devices.

To overcome the limited range of the IDMT-based models, one needs to employ the MD model, which is valid over a wide range of adhesion parameter values. To this end, Adams et al. [17] employed the MD adhesion model to model rough contacting surfaces and developed a scale-dependent friction model. In their model they only considered the adhesion from the contacting and intimately contacting asperities, ignoring the contribution from the non-contacting asperities. Morrow et al. [18] combined the MD model with the Kim et al. [8] extension for noncontacting asperities and developed a model for rough contacting surfaces that includes adhesion from the noncontacting asperities. However, both the Adams et al. [17] and Morrow et al. [18] models are valid only for elastic contacting asperities, since they directly use the MD model, which is limited to such contacts. Furthermore, these models are valid for dry contact conditions only.

In many micro/nano applications, the presence of molecularly thin lubricants either is desired or cannot be avoided. Thin lubricant can either be deliberately applied to surfaces, e.g., magnetic storage thin film disks containing a perfluoropolyether (PFPE) lubricant 1–2 nm thick, or found in devices being operated in the presence of humidity, which forms a molecularly thin water layer on the surface [19]. Stanley et al. [20] developed an adhesion model (SBL model) to take into consideration the effect of molecularly thin lubricant layers. Following the same idea, Lee [21] developed an improved SBL model (ISBL) by combining the KE dry contact adhesion model with the SBL model. As with the dry contact models, both the SBL and the ISBL models are valid for elastic–plastic contacts but limited to low adhesion parameter values. In applications involving large adhesion parameter values, they significantly underestimate adhesion, as shown in Section 3.

Another important issue that is also addressed in this paper is the adhesion instability that may occur as surfaces move into and out of contact. Refs. [9,22] discussed this phenomenon for the case of single-asperity spherical contacts, where adhesion instability results in the “jump-on” and “jump-off” phenomena during the approaching and departing processes, respectively. It was found [9] that under displacement control, the “jump-on” and “jump-off” points are the same for adhesion parameter values $\lambda < 0.95$ and different for $\lambda > 0.95$. In magnetic storage HDIs, such adhesive instabilities have been experimentally observed [23] and also numerically modeled [24]. However, the literature

on the instability of adhesive rough surfaces in contact, as far as roughness effects are concerned, is absent.

In this paper, the EMD and ISBL models were combined to obtain an improved adhesion model for rough contacting surfaces in the presence of molecularly thin lubricant. The proposed model, termed the elastic–plastic hybrid adhesion model, overcomes the difficulties of earlier models; namely, it is valid for elastic–plastic contacts and for the entire range of adhesion parameter values. Last, the instability of adhesive rough surfaces in contact is discussed based on the amplitude and the stiffness of the external force.

2. Extended Maugis–Dugdale (EMD) model for spherical contacts

2.1. Maugis–Dugdale (MD) model [7]

Maugis proposed an analytical transition between the JKR and IDMT models by combining fracture mechanics theory with the Dugdale constant stress approximation. In the MD model, the contact interface was treated as a crack and the adhesive stress was constant (σ_0) over a length of l ($l = c - a$) at the tip of the crack, where a and c are the radii of the contact and adhesive zones respectively. Fig. 1 depicts simulation results and sketches of the EMD [9]

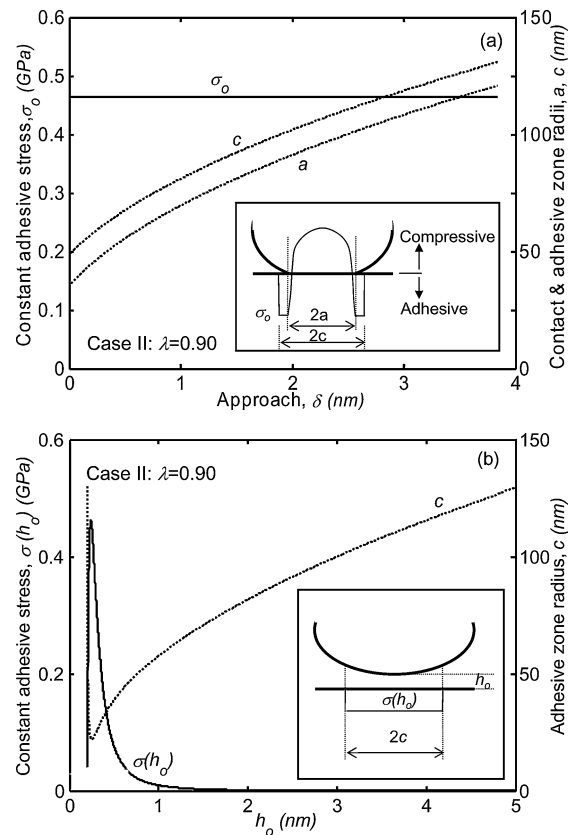


Fig. 1. Extended Maugis–Dugdale (EMD) model, Case II (single sphere): (a) contacting conditions (MD model); (b) noncontacting conditions.

single-asperity (sphere-on-flat) model using case II spherical contact parameters, listed in Table 2. The values listed in Table 2 represent realistic magnetic storage head–disk interface parameters with case I being the roughest case (vintage interface) and case III representing current HDI technology. The energy of adhesion values represents realistic HDI values due to the presence of the molecularly thin PFPE lubricant, humidity, and contamination. Fig. 1a shows the contacting conditions of the EMD model, which are the same as in the original MD model, and Fig. 1b shows the noncontacting conditions of the EMD model. Shown in Fig. 1a is the constant adhesive stress, σ_0 , which is independent of the approach δ . The inset of Fig. 1a shows a schematic representation of the stress distribution of the MD model, along with the diameters of the contact ($2a$) and adhesive ($2c$) zones. By defining parameter $m = c/a$, the MD solution gives [7]

$$\frac{\lambda A_M^2}{2} [\sqrt{m^2 - 1} + (m^2 - 2) \tan^{-1} \sqrt{m^2 - 1}] + \frac{4\lambda^2 A_M}{3} [\sqrt{m^2 - 1} \tan^{-1} \sqrt{m^2 - 1} - m + 1] = 1, \quad (1)$$

where the dimensionless contact radius

$$A_M = a \left(\frac{K}{\pi \Delta \gamma R^2} \right)^{1/3} \quad (2)$$

and λ is a dimensionless adhesion parameter given by

$$\lambda = 2\sigma_0 \left(\frac{R}{\pi \Delta \gamma K^2} \right)^{1/3}. \quad (3)$$

Note that K is related to the reduced Young's modulus E_r ($K = \frac{4}{3} E_r$; $E_r = E_1/(1 - \nu_1^2) + E_2/(1 - \nu_2^2)$), R is the asperity radius, and $\Delta \gamma$ is the energy of adhesion. Also, the dimensionless external load F_M is given by

$$F_M = \frac{F}{\pi \Delta \gamma R} = A_M^3 - \lambda A_M^2 [\sqrt{m^2 - 1} + m^2 \tan^{-1} \sqrt{m^2 - 1}] \quad (4)$$

and the dimensionless elastic approach Δ_M by

$$\Delta_M = \delta \left(\frac{K^2}{\pi^2 \Delta \gamma^2 R} \right)^{1/3} = A_M^2 - \frac{4}{3} A_M \lambda \sqrt{m^2 - 1}, \quad (5)$$

where the theoretical stress

$$\sigma_0 = 1.03 \frac{\Delta \gamma}{Z_0}. \quad (6)$$

Z_0 is the equilibrium spacing, which depends on the material lattice parameter and surface energy of the interface materials [25]. According to [25], for most surfaces, $Z_0 = 0.2$ nm, which is also adopted in this work.

Using Eqs. (1)–(6), simulations were performed using the spherical parameters for case II (Table 2), and the results show that the contact and adhesive zone radii a and c , respectively, increase nonlinearly with increasing approach, as shown in Fig. 1a. Based on the MD model, the adhesive

Table 2
Simulation parameters

Material parameters		Hardness of softer material, H (GPa)		Combined Young's Modulus, E_r (GPa)		
		2.50		85.29		
Surface parameters	Plasticity index (ψ)	η (μm^{-2})	σ (nm)	R (μm)	$\Delta \gamma$ (N/m)	λ
Case I	1.76	8.51	3.40	1.66	0.01	0.16
Case II	0.84	7.39	1.62	3.33	0.09	0.90
Case III	0.39	9.87	0.65	6.38	0.30	2.49

Note. Shaded area indicates the parameters needed for spherical (single-asperity) contact.

stresses outside and inside the contact regions are given by

$$\sigma(r) = \sigma_0 \quad \text{for } a < r < c, \quad (7a)$$

$$\sigma(r) = \sigma_0 \frac{2}{\pi} \tan^{-1} \left(\frac{c^2 - a^2}{a^2 - r^2} \right)^{1/2} \quad \text{for } r < a. \quad (7b)$$

By integrating the adhesive stresses over the overall circular area, the total adhesive force F_s is obtained as

$$F_s = \sigma_0 \pi (c^2 - a^2) + \int_0^a 2\pi r \frac{2\sigma_0}{\pi} \tan^{-1} \left(\frac{c^2 - a^2}{a^2 - r^2} \right)^{1/2} dr = 2\sigma_0 a^2 (m^2 \tan^{-1} \sqrt{m^2 - 1} + \sqrt{m^2 - 1}). \quad (8)$$

2.2. EMD model for noncontact [9]

For the case of a noncontacting asperity, following the same idea as in the MD model of assuming a constant adhesive stress, $\sigma(h_0)$, acting in a circular area of radius c (with contact radius a being zero), Shi and Polycarpou [9] extended the MD model and proposed an adhesion model that covers the full range of contact and noncontact and the associated instabilities. Based on classical contact mechanics theory, the adhesive radius c is obtained from the solution of the equation

$$\frac{c^2}{2R} + \frac{2\sigma(h_0)c(\pi - 2)}{\pi E_r} + h_0 - h_c = 0. \quad (9)$$

Also, based on the Lennard–Jones surface potential and the definition of the adhesion work, one can readily relate the normal separation at the center h_0 and the edge h_c of the adhesive zone caused by the deformation due to the presence of adhesion,

$$h_c = h_0 + \frac{1}{\sigma(h_0)} \int_{h_0}^{\infty} \sigma(z) dz, \quad (10)$$

where the adhesive stress is given by the Lennard–Jones surface potential as

$$\sigma(z) = \frac{8}{3} \frac{\Delta \gamma}{Z_0} \left\{ \left(\frac{Z_0}{z} \right)^3 - \left(\frac{Z_0}{z} \right)^9 \right\}. \quad (11)$$

Z is the deformed normal surface separation.

The schematic representation of the stress distribution for the noncontact situation is shown in the inset of Fig. 1b. Different from the MD contact asperity model shown in Fig. 1a, the adhesive stress σ in the EMD model is not independent of the separation h_0 , but instead is a function of h_0 . Specifically, $\sigma(h_0)$ follows the Lennard–Jones surface law, Eq. (11). Using the same simulation parameters as in the contact case (spherical case II, Table 2), the simulation predictions of the EMD model give the adhesive zone radius c vs minimum separation h_0 , as shown in Fig. 1b. Due to the fact that $\sigma(h_0)$ has its maximum value at a separation of about $1.2Z_0$, the adhesive zone radius c also has its minimum value at the same point. When the separation is larger than $1.2Z_0$, c increases nonlinearly with increasing separation. This is due to the Dugdale assumption of constant adhesive stress [7]. Considering a sphere positioned at large minimum separation h_0 , points with large separation are relatively less attractive, and thus the forces due to its nearer points (under the assumption of constant adhesive stress) are less dominant, resulting in a larger adhesive zone radius c . For the same sphere but at smaller h_0 , the adhesive stress of the nearest points is more dominant, resulting in smaller adhesive zone radius c . When the separation is below $1.2Z_0$, due to the sharp drop of $\sigma(h_0)$ with decreasing separation, c increases sharply.

In the EMD model, the adhesion force, F_s , and approach, δ , are given by

$$F_s = \pi \sigma c^2, \quad (12)$$

$$\delta = -\left(h_0 + \frac{2\sigma c}{E_r}\right). \quad (13)$$

Using the single-asperity EMD full-approach-range adhesion model and the parameters listed in Table 2, simulations were run to demonstrate the transition from the IDMT to JKR models for single-asperity contacts. In these simulations, three cases with adhesion parameter values of 0.16 (case I), 0.90 (case II), and 2.49 (case III), corresponding to IDMT, MD, and JKR regions, respectively, were considered [22]. The roughness parameters were measured using $20 \times 20 \mu\text{m}$ AFM scans on modern thin-film magnetic disks. Note that for the sphere-on-flat or single-asperity contact simulations, only the adhesion parameter λ , asperity radius R , adhesion energy $\Delta\gamma$, and reduced Young's modulus E_r , are required for the simulations (shaded in Table 2). The roughness parameters of σ (standard deviation of surface heights) and η (areal density of asperities) as well as the hardness H are used in conjunction with the GW rough surface model (Section 3).

As shown in Fig. 2, for all three cases, the noncontact adhesion predictions (shown as negative approach δ values) using the EMD model are very close to the IDMT solution, as both models are based on the Lennard–Jones surface potential. Furthermore, the EMD model realizes the transition from the IDMT model (Fig. 2a) to the JKR model (Fig. 2c). Specifically, when the adhesion parameter is low ($\lambda = 0.16$), the prediction of the EMD model is closer to IDMT, as

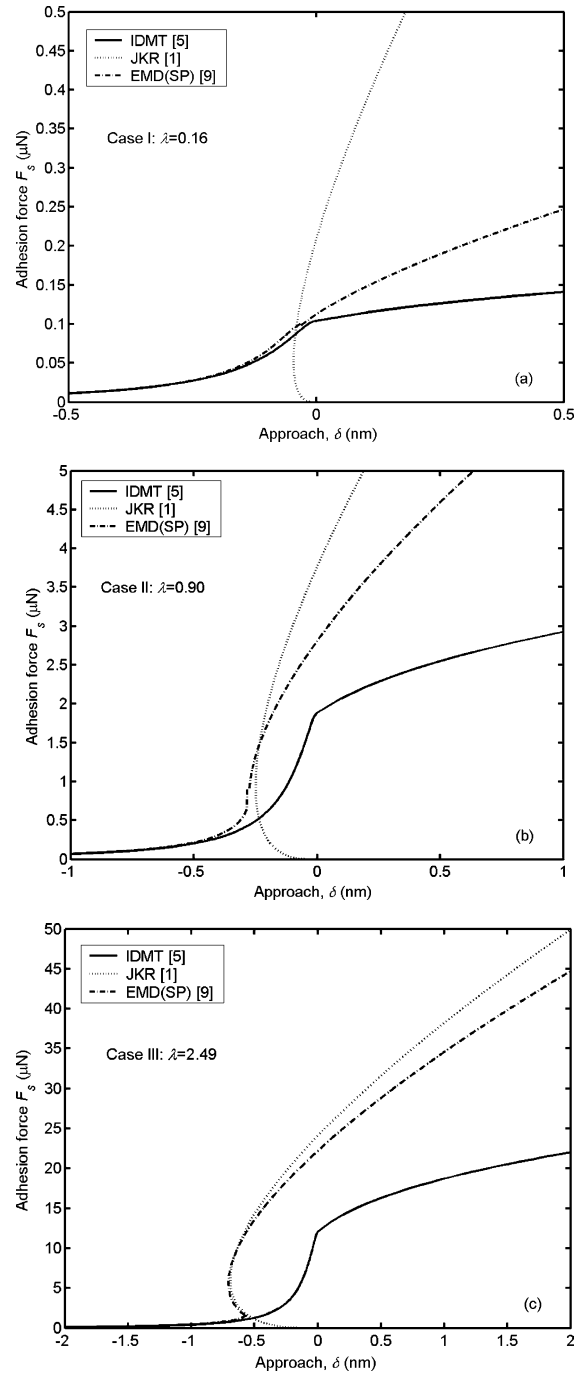


Fig. 2. Transition from IDMT to JKR models using the single-sphere EMD model: (a) case I, $\lambda = 0.16$ (IDMT); (b) case II, $\lambda = 0.90$ (MD); (c) case III, $\lambda = 2.49$ (JKR).

shown in Fig. 2a. On the other hand, when the adhesion parameter is large ($\lambda = 2.49$), the EMD solution is closer to the JKR solution, as seen in Fig. 2c. Also, Fig. 2b shows that when the adhesion parameter is well above the IDMT range, but below the JKR range ($\lambda = 0.90$), the IDMT model underestimates the adhesion force. In this range neither the JKR nor the IDMT model can accurately predict the adhesive force, and the EMD model is the only model that can accurately predict the adhesion force.

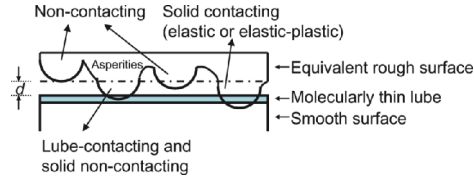


Fig. 3. GW rough surface model in the presence of molecularly thin lubricant.

3. Proposed elastic–plastic hybrid adhesion model for rough surfaces

3.1. Rough surface model

Having developed a single-asperity adhesion model that is valid for the full approach range and the full range of adhesion parameter values, one needs to extend this model to include surface roughness and also to be valid for plastically deformed asperities. The surface roughness is modeled using the Greenwood and Williamson statistical model [10], which it assumes that two rough surfaces are represented by an equivalent sum rough surface in contact with a smooth plane, as shown schematically in Fig. 3. The roughness is characterized by three parameters, namely, σ , η , R , and the asperity heights follow a Gaussian distribution, $\phi(u)$. In such a rough surface, at a certain mean separation d , some asperities will be in contact while others will be noncontacting, depending on their individual interference, ω values. Referring to Fig. 3, for a rough multiasperity contact interface, the net adhesive force is due to the individual asperity contributions, which can be grouped into four parts, namely contributions from

- (1) noncontacting asperities,
- (2) lube-contacting but solid noncontacting asperities,
- (3) elastic contacting asperities,
- (4) elastic–plastic contacting asperities.

According to the GW model, the state of elastic–plastic deformation is characterized with a plasticity index, defined as

$$\psi = \frac{2E_r}{\pi k H} \sqrt{\frac{\sigma}{R}}, \quad (14)$$

where k is a maximum contact pressure factor related to the Poisson ratio ν ($k = 0.454 + 0.41\nu$) [15]. When $\psi < 0.6$ the contact is purely elastic, for $\psi > 1$ the contact is fully plastic, and when $0.6 < \psi < 1$ the contact is elastic–plastic.

3.2. Elastic EMD model for rough surfaces

In the case of purely elastic contacts (i.e., $\psi < 0.6$), only the first three parts of the adhesive contributions need to be considered. These are the noncontacting (1), elastic contacting (2), and lube contacting (3) asperities. In the case of (1) and (2), the EMD model [9] is readily applicable, and is valid for the entire adhesion parameter range. For the lube-contacting but solid noncontacting asperities (3), the Stanley

et al. (SBL) model [20] is adopted, as it accounts for the presence of a molecularly thin lubricant layer. The statistical sum of the three contributions gives the elastic EMD model for rough surfaces. Thus the total net adhesion force F_s is obtained as

$$F_s = A_n \eta \left\{ \int_{-\infty}^{d-t-\delta_A} f_{\text{snc}} \phi(u) du + \int_{d-t-\delta_A}^{d-\delta_A} f_{\text{slc}} \phi(u) du + \int_{d-\delta_A}^{d+\omega_c} f_{\text{sel}} \phi(u) du \right\}, \quad (15)$$

where A_n is the nominal contact area, d is the mean surface separation, t is the lubricant thickness, u is the asperity height, and ω_c is the critical interference at the inception of plastic deformation and is directly related to the plasticity index ($\omega_c = \sigma/\psi^2$).

The first and third integrals, f_{snc} , f_{sel} , represent the contributions from the individual noncontacting and elastically contacting asperities, respectively, and could be directly obtained from the EMD model. However, due to the complexity of the EMD formulation, the functions f_{snc} , f_{sel} as used in Eq. (15) are analytical functions obtained from curve-fitting the EMD numerical results, using the methodology described in Appendix A. Basically the numerical solution of the MD and EMD Eqs. (1)–(13) for a single asperity as a function of approach (for specific parameters of R , λ , $\Delta\gamma$, and Z_0) are curve-fitted with nonlinear functions using a least-squares method. As described in Appendix A, these functions have complex forms in order to obtain a fitting error of less than 1%, compared to the numerical results. Using this method, force expressions as a function of approach, e.g., $f_{\text{snc}}(\delta)$, are obtained, so that they can be directly applied to the multiasperity GW rough surface model (Eq. (15)). Note that curve-fitting the MD model was also proposed in Refs. [18,26,27]. However, unlike our approach, which directly fits the force–approach relationships, in their method they separately curve fitted the force and approach, which are functions of the adhesion parameter λ .

According to Stanley et al. [20], for the individual solid noncontacting and lube-contacting asperities (second integral in Eq. (15)), the adhesive force is calculated using a truncated sphere on a flat and is equal to the adhesion at a point-contact situation, i.e.,

$$f_{\text{slc}} = 2\pi \Delta\gamma R. \quad (16)$$

In the absence of molecularly thin lubricant (i.e., dry contact), Eq. (15) is still applicable by setting the lubricant thickness $t = 0$ and dropping the f_{slc} term. Details of the SBL and ISBL models are given in Appendix B.

δ_A in Eq. (15) is a critical approach parameter, which is due to the “necking” phenomenon observed when a sphere approaches (or departs from) a surface. As discussed in Refs. [9,22], due to this instability and the necking phenomenon, the contact will be initiated at a negative approach and not

at a zero approach. In rough surface adhesive modeling δ_A is usually ignored; however, it is considered in this paper, where for a specific material pair, the value of δ_A is obtained using Eqs. (23) and (25) from Ref. [9]. Typical δ_A values are several angstroms.

As discussed in Section 2 for single-asperity contacts, when the value of the adhesion parameter is large, the IDMT model significantly underestimates the adhesion force. Similarly, for large adhesion parameter values, when the single-asperity IDMT model is used to develop a rough surface model, namely the SBL and ISBL models, then when the contacting asperities make a significant contribution to adhesion, which is the case once contact occurs, the model will also underestimate the total adhesion force. In this situation, the rough surface EMD model is applicable and will give more accurate results.

3.3. Hybrid elastic–plastic adhesion model for rough surfaces

As discussed earlier, the EMD model is only valid for elastic contacts, while it is expected that in a rough surface contact, some asperities will also be plastically deforming. If the contact is plastic or elastic–plastic, the rough surface EMD model (Eq. (15)) will underestimate the adhesion forces. Therefore, it is important to also include the adhesion contribution from the plastically deformed asperities. In this work, the rough surface EMD model was combined with the KE model [16] to obtain an adhesion model (termed the elastic–plastic hybrid adhesion model) that in addition to being valid for the full range of adhesion parameters is also valid for elastic–plastic and fully plastic conditions. The total adhesion force F_s is then the statistical sum from the contribution of all four types of asperities and is given by

$$F_s = A_n \eta \left\{ \int_{-\infty}^{d-t-\delta_A} f_{\text{sncl}} \phi(u) du + \int_{d-t-\delta_A}^{d-\delta_A} f_{\text{slcl}} \phi(u) du + \int_{d-\delta_A}^{d+\omega_c} f_{\text{sel}} \phi(u) du + \int_{d+\omega_c}^{d+6\omega_c} f_{\text{selpl1}} \phi(u) du + \int_{d+6\omega_c}^{d+110\omega_c} f_{\text{selpl2}} \phi(u) du \right\}. \quad (17)$$

The last two terms in Eq. (17) represent the contribution from the elastic–plastic deformed asperities and the integrands f_{selpl1} and f_{selpl2} are given by [16]

$$f_{\text{selpl1}} = 1.58\pi R \Delta \gamma \left(\frac{u-d}{\omega_c} \right)^{0.356} \left(\frac{Z_0}{\omega_c} \right)^{-0.321}, \quad (18)$$

$$f_{\text{selpl2}} = 2.38\pi R \Delta \gamma \left(\frac{u-d}{\omega_c} \right)^{0.093} \left(\frac{Z_0}{\omega_c} \right)^{-0.332}. \quad (19)$$

Further details of the KE model are given in Appendix B.

4. Simulation results

To demonstrate the applicability of the rough surface elastic EMD model, simulations were initially run using case III parameters (Table 2), which represent elastic contact conditions (plasticity index $\psi = 0.39$) and a large adhesion parameter value of $\lambda = 2.49$. Under these conditions, the elastic EMD model given by Eq. (15) is valid (elastic contacts only), whereas the SBL and ISBL models will underestimate the adhesion force since λ is large. The simulation results using the EMD, SBL, and ISBL models are shown in Fig. 4 and it is clearly seen that the elastic EMD model predicts higher adhesion, which verifies the underestimation of the SBL and ISBL models. Note also that the predictions of the SBL and ISBL models are very similar since the contact is purely elastic.

Simulations were next performed using the proposed hybrid adhesion model and all the rough surface simulation parameters listed in Table 2. As discussed in Section 2, the three cases listed in Table 2 cover a large range of the adhesion parameter λ . Furthermore, they also represent elastic, elastic–plastic, and plastic contact conditions, as characterized by the plasticity index values.

In the simulations, the ISBL rough surface adhesion model is compared with the proposed elastic EMD rough surface model and the more general elastic–plastic hybrid model, as shown in Figs. 5a–5c for cases I–III, respectively. Before contact, at mean normal separations h larger than 3σ for cases I and II and larger than 5σ for case III, the adhesion estimates are similar for all models, since all models are based on the Lennard–Jones potential. After contact (where the onset of contact occurs at 3σ , or at $h^* = 3$ due to the statistical nature of the roughness), adhesion increases rapidly with decreasing mean normal separation and the three models predict different adhesion as the contacting asperities significantly contribute to adhesion.

Referring to Fig. 5a, when λ is small, the proposed hybrid rough surface model gives results very close to the ISBL

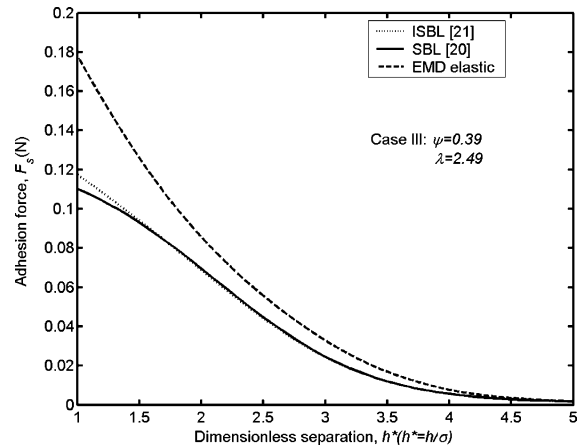


Fig. 4. Rough surface adhesive contact—comparison between elastic EMD, SBL, and ISBL models. Case III, predominantly elastic contact with high adhesion parameter value.

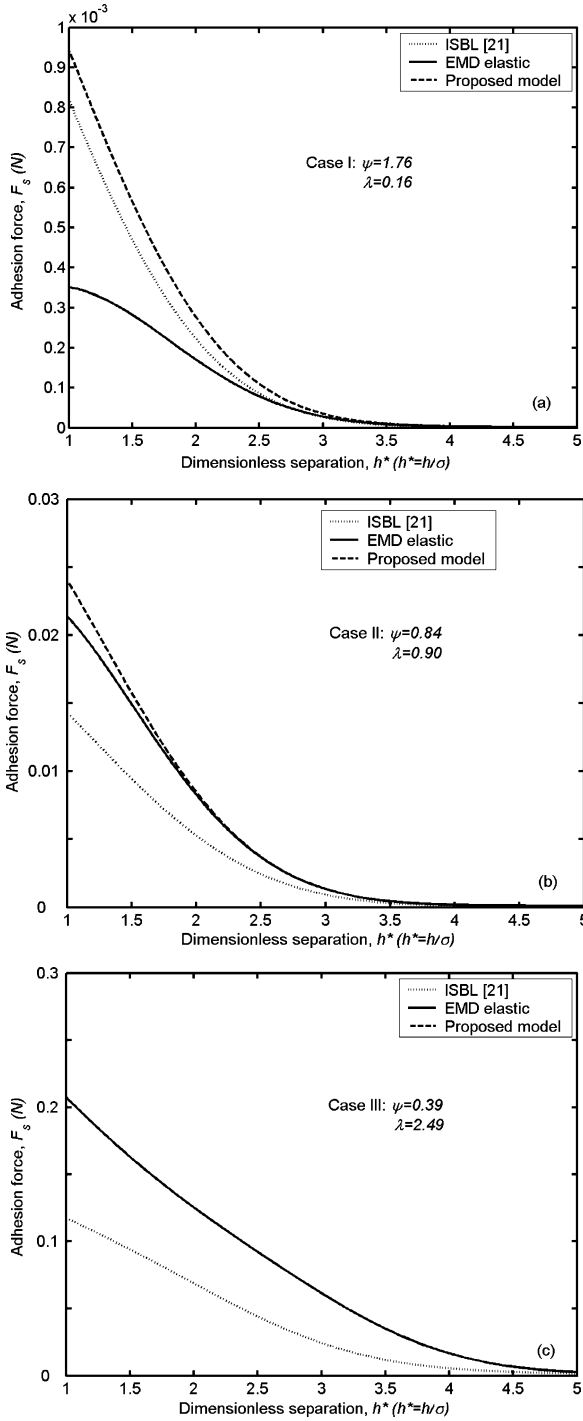


Fig. 5. Rough surface adhesive contact—comparison between elastic EMD, ISBL, and hybrid elastic–plastic EMD models: (a) case I; (b) case II; (c) case III.

model, which is based on the IDMT model. This is in agreement with the findings of single-asperity contact modeling, in which case when λ is small (in the range of the IDMT model), the EMD model predicts adhesion similar to that in the IDMT model. However, when λ is well above the IDMT range, the IDMT model underestimates adhesion for both single-asperity contacts (discussed in Fig. 2), as well as

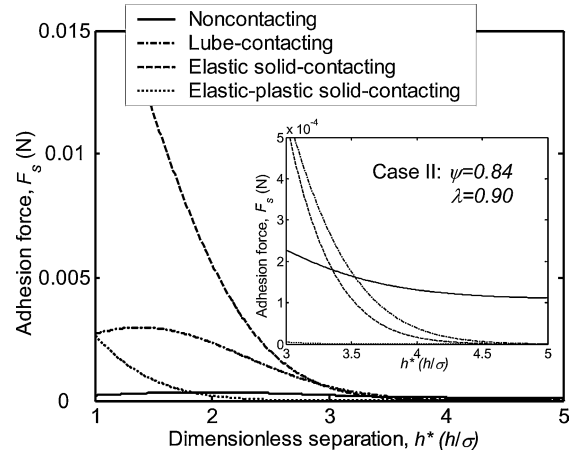


Fig. 6. Rough surface adhesive contact—adhesive contributions from different asperity groups using the hybrid elastic–plastic EMD model, case II.

for the case of rough surface contact, as shown in Figs. 5b and 5c.

Also shown in Figs. 5a–5c is the comparison between the elastic EMD model and the proposed elastic–plastic hybrid model. As expected, for elastic contact conditions, as is the case in Fig. 5c, the adhesive force estimates using the elastic EMD model are identical to the estimates of the proposed elastic–plastic model (the two models are indistinguishable in the figure). However, for elastic–plastic contact conditions such as the case depicted in Fig. 5a, the EMD elastic model significantly underestimates the adhesion force, especially with significant asperity contact. Notice that case II, which involves some plastic deformation ($\psi = 0.84$), both elastic and elastic–plastic hybrid models give similar results.

Fig. 6 shows the individual adhesion contributions from the different asperity groups as represented by the different integrals in the elastic–plastic hybrid model, Eq. (17) (case II in Table 2). As shown in the inset of Fig. 6, before contact (i.e., $h^* > 3$), the contribution from the noncontacting asperities dominates the adhesion behavior, as expected. Once contact is initiated ($h^* < 3$), the elastic contacting asperities become dominant. The lube-contacting asperities have the second highest significant contribution under contact conditions. The contribution of the elastic–plastic asperities becomes important only with very heavy contacts ($h^* < 2$).

The above discussion is in terms of adhesive forces, which provide physical insight to the rough surface adhesive problem. However, in practical applications, the external force is usually readily measured and thus it is practically more relevant to discuss adhesive problems in terms of the external force. This issue, along with the instability issue associated with in-contact and out-of-contact transitions, is discussed in Section 5.

5. Instabilities for adhesive rough contacting surfaces

Even though instabilities associated with adhesive spherical (single asperity) contacts have been investigated in the

literature, e.g., [9,22], the literature on the instability of adhesive rough surfaces is scarce. Recent technological advances in magnetic storage HDIs necessitated the recording slider being in extremely close proximity to the rotating magnetic disk, on the order of sub-5-nm spacing. Under such low-spacing conditions it has been experimentally observed that adhesive instabilities occur, causing the HDI to become unstable. Furthermore, it has been observed that the presence of adhesion at the HDI causes a hysteresis phenomenon, where the magnitude of the interfacial forces is different during touchdown (approach) and takeoff (departure) processes [23]. These instabilities have been investigated from the system dynamics point of view, e.g., numerically using an advanced air-bearing simulator (no roughness effects) [24]. However, none of the literature specifically investigated adhesive instability in terms of the roughness effects.

A major difficulty in investigating adhesive instability in rough surfaces is the difficulty in defining the onset of contact in contacting rough surfaces. Recall that in the case of single spherical contacts or the contact of infinitely smooth surfaces, contact was defined as taking place when the two continuum surfaces were apart by a distance equal to Z_0 (equilibrium spacing). A similar definition does not exist for rough surfaces; the definition of the onset of contact needs to be done in a statistical sense, as the asperity heights are not constant but follow a certain distribution. Next, the instability for adhesive rough surfaces contact is discussed based on external force behavior.

Before the related rough surface instabilities are discussed, the calculation of the external force needs to be addressed. In previous sections, the calculation of the adhesion force (F_s) has been presented. Similarly, one can calculate the contact force P , and then the external force F can be obtained as $F = P - F_s$. Similar to the adhesion calculation, the contacting asperities are also divided into two groups in order to calculate the contact force. One is for the elastically deforming asperities and the other for both elastically-plastically and fully plastically deforming asperities. For the elastic asperities, based on the MD model [7], the contact force is given by

$$P_{el} = \int_d^{d+\omega_c} f_{sel}\phi(u) du + \int_d^{d+\omega_c} f_f\phi(u) du, \quad (20)$$

where f_f is a curve-fitted analytical equation for the external force based on the MD model (see Appendix A). For elastic-plastic and fully plastic asperities, the contact force is obtained by [16]

$$P_{elpl} = \frac{2}{3}\pi\eta Rk\omega_c A_n H \left\{ 1.03 \int_{d+\omega_c}^{d+6\omega_c} I^{1.425} + 1.4 \int_{d+6\omega_c}^{d+110\omega_c} I^{1.263} + \frac{3}{k} \int_{d+110\omega_c}^{\infty} I^1 \right\}, \quad (21)$$

where

$$I^b = \left(\frac{u-d}{\omega_c} \right)^b \phi(u) du. \quad (22)$$

Thus, from Eqs. (17) and (20)–(22), the total external force, F , is given by

$$F = P_{el} + P_{elpl} - F_s. \quad (23)$$

As shown in Fig. 7a, for different adhesion and roughness levels, the magnitude of the external forces given by Eq. (23) varies significantly, even though they all exhibit similar behavior (case II is also shown in the inset, with case I having similar behavior). For the intermediate case II ($\sigma = 1.619$ nm and $\Delta\gamma = 0.09$ N/m), the pull-off force (defined as the minimum external force) is only 0.6 mN, whereas for the smoother case III ($\sigma = 0.6541$ nm and $\Delta\gamma = 0.30$ N/m), the pull-off force is much higher, 93.5 mN (for the roughest case I, the pull-off force is insignificantly small, 2.13 μ N). For case III, the line of $h = 2$ nm ($h^* = 3.06$) shows the point where the external force has the largest slope, which corresponds to the peak value of the stiffness,

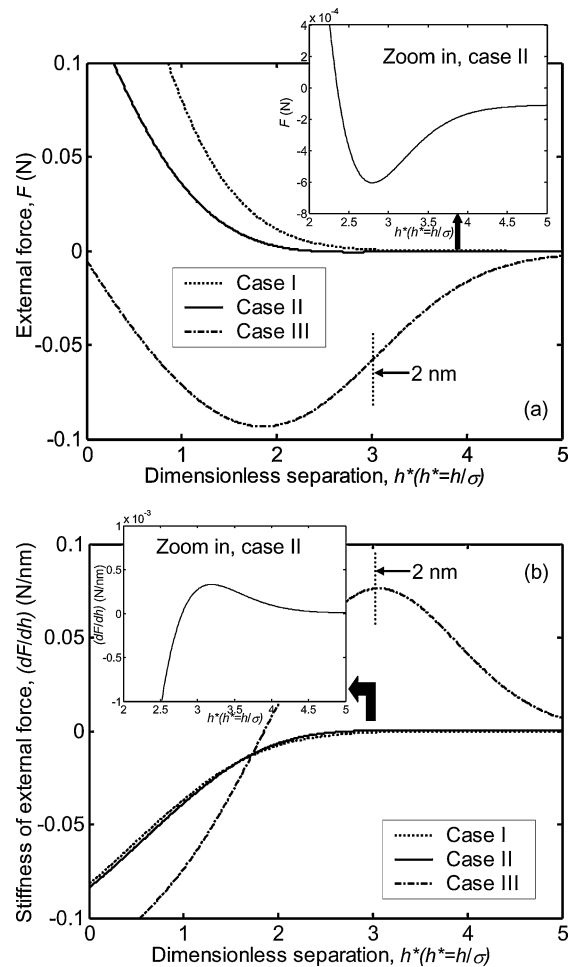


Fig. 7. Rough surface adhesive contact—roughness and adhesion levels effects (case I: $\sigma = 3.4$ nm, $\Delta\gamma = 0.01$ N/m; case II: $\sigma = 1.619$ nm, $\Delta\gamma = 0.09$ N/m; case III: $\sigma = 0.6541$ nm, $\Delta\gamma = 0.30$ N/m.) (a) Amplitude of external force; (b) stiffness of external force.

as also clearly shown in Fig. 7b. With larger adhesion, the stiffness of the external force has a larger peak value, which may cause the contact process to become unstable. Examining Figs. 7a and 7b, the highest stiffness for the smoothest case of $\sigma = 0.6541$ nm and $\Delta\gamma = 0.3$ N/m occurs at a surface separation of 2 nm ($\approx 3.06\sigma$). This means that when the two surfaces come into contact at this specific point, the adhesion increases sharply, and thus the external force sharply decreases. Consequently, if there is no other force in the system that is sufficiently large to counterbalance this negative external force, the surfaces will approach each other very fast (“snap” to contact) and the contact process will become unstable. For the rougher cases I and II, the corresponding dimensionless separations where the maximum stiffness occur are further away from the onset of contact condition at $h^* = 5.72$ and 3.19, respectively. Furthermore, as their corresponding pull-off forces are very small, the possibility of unstable behavior is also very small.

As seen in Fig. 7, the pull-off force and the adhesion instability are greatly affected by the surface roughness σ and the surface energy $\Delta\gamma$. The effect of surface roughness on the pull-off force has also been discussed by Stanley et al. [20]. They investigated rougher surfaces compared to the present study with $\sigma = 11.4$ –286 nm, and they reported that smoother surfaces result in higher adhesion, and the pull-off force position also occurs at a smaller dimensionless surface separation, which is in agreement with this work.

To specifically investigate the effect of surface energy on the external force and associated instability, we consider the smoothest case III roughness parameters (extremely smooth interface), which represent current HDI technology. In these simulations, depicted in Fig. 8, the surface energy values range from 0.04 to 0.14 N/m, which represent realistic HDI cases, with 0.04 N/m representing PFPE lubricant and 0.14 N/m high humidity levels. Unlike the order-of-magnitude difference in the pull-off forces with roughness variations discussed in Fig. 7, the effect of the surface energy (within the practical HDI range) is smaller, with pull-off force values of 6.3, 19.9, and 35.8 mN for $\Delta\gamma = 0.04, 0.09,$

and 0.14 N/m, respectively. Also, the corresponding locations of the maximum pull-off force stiffness are similar and are $h^* = 2.82, 2.75,$ and 2.80. In typical HDI applications, under steady-state conditions, the external applied force (or preload) is typically counterbalanced by the generated air-bearing lift force and the magnitude of these forces is around 10 mN. Thus, when the pull-off force and its rate of change (stiffness) are significantly large (comparable to the preload), the system will easily become unstable under an external disturbance. As seen in Fig. 8, for the supersmooth HDI (case III), the adhesion instability is important, especially at high humidity levels ($\Delta\gamma = 0.14$ N/m).

6. Summary

Despite significant advances in modeling and understanding single-asperity adhesion and associated instabilities, understanding of such phenomena for rough surfaces in contact has not advanced as much. As miniature systems such as magnetic storage devices and MEMS continue to advance, the need to understand realistic adhesive contact phenomena (including roughness effects) is vital to the successful design and reliability of these devices. Based on one of the classical single-asperity adhesion models (the IDMT model, which is valid for both noncontact and contact conditions), several rough surface adhesion models have been proposed using the GW statistical roughness model. These include the CEB/KE (dry contact) and SBL/ISBL (molecularly thin lubricated contact) elastic–plastic models. Also, based on the elastic MD single-asperity model, researchers have proposed rough surface adhesion models, which are valid for elastic contacts. The existing adhesion models are either only valid for elastic contact (MD-based) or only valid for applications with small adhesion parameter values (IDMT-based).

In this paper, an elastic MD rough-surface model and an elastic–plastic hybrid model were proposed that are valid for a wide range of adhesion parameter values. Simulation results using the proposed models were compared to the ISBL model and showed similar results for low adhesion parameter values. Furthermore, the simpler elastic model gives results similar to those for the elastic–plastic model when the contact, as characterized by the plasticity index, is predominantly elastic. Last, the instability during the rough-surfaces contact process was discussed based on the external force and its rate of change with mean normal separation. It was found that the peak value of the stiffness (directly obtained from the external force) is related to the instability of the contacting process.

Acknowledgment

This research was supported by the National Science Foundation under Grant CAREER CMS-0239232. The authors gratefully acknowledge this support.

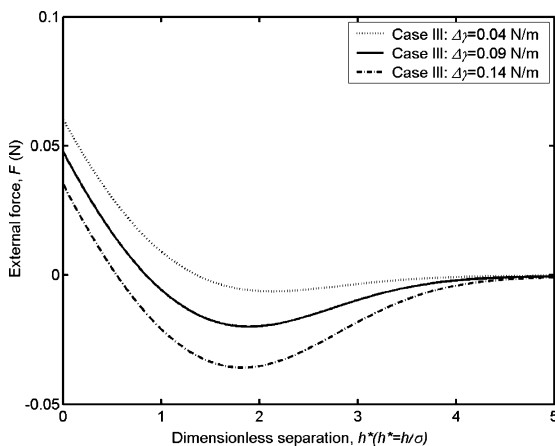


Fig. 8. Rough surface adhesive contact—effect of surface energy on the external force, case III, supersmooth HDI.

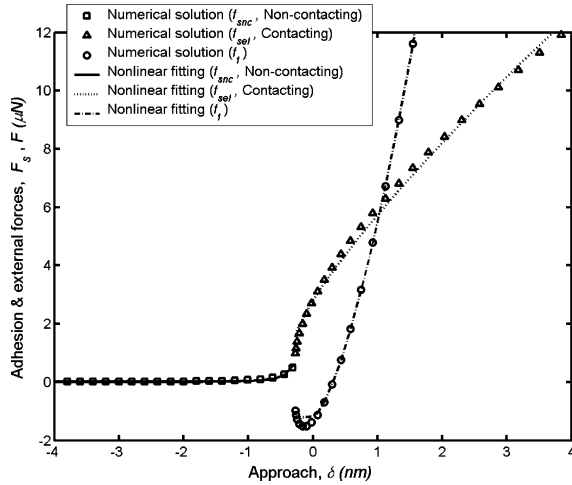


Fig. 9. Nonlinear least-squares fitting of forces for sphere-on-flat as a function of approach (case II).

Appendix A. Curve-fitted simplified solutions of EMD single-asperity model

In order to directly apply the single-asperity MD and EMD models to rough surfaces in contact, analytical expressions for the adhesive and external forces as a function of the approach and surface/material parameters are needed. However, the complexity of the MD/EMD models makes it impossible to obtain such analytical solutions. To overcome this problem, a nonlinear least-squares fitting methodology was adopted in this work.

For a specific material pair, the parameters E , R , $\Delta\gamma$, and Z_0 are known and one can readily obtain the numerical solution to the MD/EMD models using Eqs. (1)–(13). From the solution, all the relevant forces, namely the noncontacting adhesion, contacting adhesion, and contacting external force, can be obtained as a function of normal approach. Then, using a nonlinear square fit method, analytical functions were obtained for these forces as a function of approach. The numerical results of the noncontacting adhesion, f_{snc} , contacting adhesion, f_{sel} , and external force, f_f , are represented very well by the functions

$$f_{snc} = f_{sonc} + \frac{2A_{nc}}{\pi} \frac{B_{nc}}{4(\delta - \delta_{onc})^2 + B_{nc}^2}, \quad (\text{A.1a})$$

$$f_{sel} = f_{soc} + (A_c\delta + B_c)^{P_c}, \quad (\text{A.1b})$$

$$f_f = f_{f0} + A_f\delta^{m_f} + B_f\delta^{n_f}, \quad (\text{A.1c})$$

where f_{sonc} , A_{nc} , B_{nc} , δ_{onc} , f_{soc} , A_c , B_c , P_c , f_{f0} , A_f , B_f , m_f , and n_f are fitting coefficients. In all cases, the fitting error was less than 1%. Typical curve-fitted functions for the adhesion and external forces for the roughness case II are shown in Fig. 9 and the corresponding fitting coefficients for this case along with cases I and III are listed in Table 3.

Table 3
Fitting coefficients to MD/EMD approximations

	Case I	Case II	Case III
f_{sonc}	2.300×10^{-4}	1.400×10^{-2}	1.818×10^{-2}
A_{nc}	8.015×10^{-2}	7.083×10^{-1}	9.649×10^0
B_{nc}	3.153×10^{-1}	2.202×10^{-1}	2.563×10^{-1}
δ_{onc}	9.125×10^{-2}	-1.324×10^{-1}	-6.358×10^{-2}
f_{soc}	6.662×10^{-2}	1.648×10^0	1.962×10^1
A_c	1.338×10^{-1}	4.514×10^0	2.644×10^1
B_c	9.780×10^{-3}	1.170×10^0	3.181×10^0
P_c	6.676×10^{-1}	8.100×10^{-1}	7.992×10^{-1}
f_{f0}	-7.041×10^{-2}	-1.193×10^0	-7.579×10^0
A_f	2.323×10^0	3.341×10^0	4.796×10^0
B_f	2.323×10^0	3.341×10^0	4.796×10^0
m_f	1.498×10^0	1.489×10^0	1.468×10^0
n_f	1.498×10^0	1.489×10^0	1.476×10^0

Appendix B. SBL [20] and ISBL [21] models

Stanley et al. [20] developed an adhesion model that includes the presence of a molecularly thin lubricant layer in a rough interface. The model is based on the IDMT single-asperity model and the total adhesion force is given by

$$F_s = \frac{8}{3}\pi\eta R A_n \Delta\gamma Z_0^2 \left\{ \int_{-\infty}^{d-t} \left[\frac{1}{(Z_0 - u + d - t)^2} - \frac{0.25Z_0^6}{(Z_0 - u + d - t)^8} \right] \phi(u) du + \frac{3}{4Z_0^2} \int_{d-t}^d \phi(u) du + \frac{2}{R} \int_d^{\infty} \int_0^{\infty} \left[\frac{1}{(u - d - t)^3} - \frac{Z_0^6}{(u - d - t)^9} \right] \times s\phi(u) du ds \right\}, \quad (\text{B.1})$$

where the three integrals represent the noncontacting, lube-only contacting, and elastic/plastic contacting asperities, respectively. Kogut and Etsion [16] developed an adhesion model for rough surfaces under dry contact conditions. Subsequently, Lee [21] combined the SBL model with the KE model and obtained a more accurate rough-surface adhesion model that specifically includes the presence of a molecularly thin lubricant and improved elastic/plastic behavior of the asperities. The model, termed the improved SBL (ISBL) model, is given by

$$F_s = 2\pi\eta R A_n \Delta\gamma \left\{ \int_{-\infty}^{d-t} J_{nc} + \int_{d-t}^d J_{lc} + 0.98 \int_d^{d+\omega} J_{-0.29}^{0.298} + 0.79 \int_{d+\omega}^{d+6\omega} J_{-0.321}^{0.356} + 1.19 \int_{d+6\omega}^{d+11\omega} J_{-0.332}^{0.093} \right\}, \quad (\text{B.2})$$

where the first, second and third integrals correspond to noncontacting, lube-only contacting and elastic contacting

asperities. The fourth and fifth integrals correspond to plastically deformed asperities and the integrands are given by

$$J_{nc} = \frac{4}{3} \left[\left(\frac{\varepsilon}{\varepsilon - u + d - t} \right)^2 - 0.25 \left(\frac{\varepsilon}{\varepsilon - u + d - t} \right)^8 \right] \phi(u) du, \quad (\text{B.3})$$

$$J_{lc} = \phi(u) du, \quad (\text{B.4})$$

$$J_c^b = \left(\frac{u-d}{\omega_c} \right)^b \left(\frac{\varepsilon}{\omega_c} \right)^c \phi(u) du. \quad (\text{B.5})$$

References

- [1] K.L. Johnson, K. Kendall, A.D. Roberts, Proc. R. Soc. London Ser. A 324 (1971) 301.
- [2] B.V. Derjaguin, V.M. Muller, Y.P. Toporov, J. Colloid Interface Sci. 53 (1975) 314.
- [3] D. Tabor, J. Colloid Interface Sci. 58 (1977) 2.
- [4] V.M. Muller, V.S. Yushchenko, B.V. Derjaguin, J. Colloid Interface Sci. 77 (1980) 91.
- [5] V.M. Muller, V.S. Yushchenko, B.V. Derjaguin, J. Colloid Interface Sci. 92 (1983) 92.
- [6] L. Kogut, I. Etsion, J. Colloid Interface Sci. 261 (2003) 372.
- [7] D. Maugis, J. Colloid Interface Sci. 150 (1992) 243.
- [8] K.S. Kim, R.M. McMeeking, K.L. Johnson, J. Mech. Phys. Solids 46 (1998) 243.
- [9] X. Shi, A.A. Polycarpou, J. Colloid Interface Sci. 281 (2005) 449.
- [10] J.A. Greenwood, J.B.P. Williamson, Proc. R. Soc. London Ser. A 295 (1966) 300.
- [11] I. Etsion, M. Amit, ASME J. Trib. 115 (1993) 406.
- [12] A.A. Polycarpou, I. Etsion, STLE Trib. Trans. 41 (1998) 217.
- [13] A.Y. Suh, A.A. Polycarpou, ASME J. Trib. 125 (2003) 193.
- [14] J.A. Greenwood, in: I.L. Singer, H.M. Pollock (Eds.), Fundamentals of Friction: Macroscopic and Microscopic Processes, Kluwer Academic, Dordrecht, 1992, p. 37.
- [15] W.R. Chang, I. Etsion, D.B. Bogy, ASME J. Trib. 110 (1988) 50.
- [16] L. Kogut, I. Etsion, ASME J. Trib. 126 (2004) 34.
- [17] G.G. Adams, S. Müftü, N.M. Azhar, ASME J. Trib. 125 (2003) 700.
- [18] C. Morrow, M. Lovell, X. Ning, J. Phys. D Appl. Phys. 36 (2003) 534.
- [19] Y. Li, D. Trainer, F.E. Talke, IEEE Trans. Magn. 26 (1990) 2487.
- [20] H.M. Stanley, I. Etsion, D.B. Bogy, ASME J. Trib. 112 (1990) 98.
- [21] S.C. Lee, Microtribodynamics of Sub-Five Nanometers Flying Head–Disk Interfaces in Magnetic Storage, Ph.D. thesis, University of Illinois at Urbana–Champaign, 2004.
- [22] K.L. Johnson, J.A. Greenwood, J. Colloid Interface Sci. 192 (1997) 326.
- [23] R.H. Wang, V. Nayak, F.Y. Huang, W. Tang, F. Lee, ASME J. Trib. 123 (2001) 561.
- [24] B.H. Thornton, D.B. Bogy, IEEE Trans. Magn. 39 (2003) 2420.
- [25] N. Yu, A.A. Polycarpou, J. Colloid Interface Sci. 278 (2004) 428.
- [26] O. Piétrement, M. Troyon, J. Colloid Interface Sci. 226 (2000) 166.
- [27] R.W. Carpick, D.F. Ogletree, M.J. Salmeron, J. Colloid Interface Sci. 211 (1999) 395.